Science Bulletin 64 (2019) 968–975

Contents lists available at ScienceDirect

Science Bulletin

journal homepage: www.elsevier.com/locate/scib

Article

An efficient bifunctional electrocatalyst derived from layer-by-layer self-assembly of a three-dimensional porous Co-N-C@graphene

Shichang Cai [a], Rui Wang [a], William M. Yourey [b], Junsheng Li [a], Haining Zhang [a], Haolin Tang [a,*]

[a] State Key Laboratory of Advanced Technology for Materials Synthesis and Processing, Wuhan University of Technology, Wuhan 430070, China
[b] College of Engineering, Penn State University, Hazleton, PA 18202, USA

ARTICLE INFO

Article history:
Received 26 March 2019
Received in revised form 13 April 2019
Accepted 13 May 2019
Available online 23 May 2019

Keywords:
Oxygen reduction reaction
Cobalt
Three-dimensional
Oxygen evolution reaction
Graphene

ABSTRACT

Three-dimensional (3D) porous carbon-based materials with tunable composition and microstructure are of great interest for the development of oxygen involved electrocatalytic reactions. Here, we report the synthesis of 3D porous carbon-based electrocatalyst by self-assembling Co-metal organic frameworks (MOF) building blocks on graphene via a layer-by-layer technique. Precise control of the structure and morphology is achieved by varying the MOF layer to tune the electrocatalytic properties. The as-produced electrocatalyst exhibits an excellent catalytic activity for the oxygen reduction reaction in 0.1 mol L^{-1} KOH, showing a high onset potential of 0.963 V vs. reversible hydrogen electrode (RHE) and a low tafel slope of 54 mV dec^{-1}, compared to Pt/C (0.934 V and 52 mV dec^{-1}, respectively). Additionally, it shows a slightly lower potential vs. RHE (1.72 V) than RuO_2 (1.75 V) at 10 mA cm^{-2} in an alkaline electrolyte. A rechargeable Zn-air battery based on the as-produced 3D porous catalyst demonstrates a high peak power density of 119 mW cm^{-2} at a cell voltage of 0.578 V while retaining an excellent stability over 250 charge-discharge cycles.

1. Introduction

The electrochemical oxygen reduction reaction (ORR) and oxygen evolution reaction (OER) are of great importance to a number of energy conversion devices, such as fuel cells and metal-air batteries [1]. However, the performance of these devices is significantly restricted by the sluggish kinetics of ORR/OER [2]. To date, the most commonly used ORR/OER electrocatalysts largely rely on noble metals [3], for example, platinum (Pt)-based nanocomposites are the most efficient ORR electrocatalysts, and precious ruthenium (Ru)- and iridium (Ir)-based nanocomposites are used in commercial devices for OER process [4,5]. Beyond the concerns on cost and natural abundance, these noble metal catalysts suffer from poor long-term stability. Therefore, development of affordable electrocatalysts with improved ORR/OER activities is needed for the practical application of efficient energy conversion devices [6].

Recently, enormous efforts have been devoted to developing carbon-based materials as alternative oxygen electrocatalysts [7–12]. Graphene based electrocatalysts have attracted broad attention because of their high specific surface area and good electrical conductivity [13–15]. However, graphene itself has limited ORR/OER activity in terms of onset potentials [16–21]. A possible strategy is to integrate graphene with other active components to improve the overall catalytic activity [22]. In this regard, metal–organic frameworks (MOFs) are featured by their high porosity, large surface area, and abundant active sites for redox reactions, therefore, they have been used as a precursor to yield heteroatom doped carbon electrocatalysts [23–27]. Indeed, various MOF/graphene composites demonstrate ORR/OER activities comparable to commercial noble metal based catalysts. In these hybrid systems, graphene prevents the undesired agglomeration of MOF precursors during carbonization, thus promoting the dispersion of MOF. Moreover, graphene and carbon derived from MOF yields a synergistic effect and facilitates the catalytic reaction involving oxygen [28]. Thus far, the majority of MOF/graphene hybrids are prepared by in situ growth of MOF on graphene based on a hydrothermal reaction [29–32]. Such synthesis requires rigorous reaction conditions, making the control in morphology and composition very difficult. There is certainly a need to simplify the synthesis so that the composition of the final product can be easily tuned. Additionally, an electrode with a 3D porous structure that can offer more active sites and ample channels for the reactants is ideal for the search of excellent oxygen electrocatalysts [33].

Here, we report a facile synthesis of MOF/graphene precursor for the development of an efficient bi-functional oxygen electrocatalyst. The as-produced graphene acts as a highly conductive substrate with the surface bonded with MOF building blocks.

* Corresponding author.
E-mail address: thln@whut.edu.cn (H. Tang).

https://doi.org/10.1016/j.scib.2019.05.020
2095-9273/

The as-produced catalyst exhibits a high onset potential of ~0.963 V (vs. reversible hydrogen electrode, RHE) and a current density of 5.5 mA cm^{-2} at a scanning rate of 5 mV s^{-1} and a rotating rate of 1,600 r min^{-1}). Moreover, this catalyst demonstrates a high OER activity with a potential of 1.72 V (vs. RHE) at 10 mA cm^{-2}. A Zn-air battery based on this catalyst demonstrates excellent stability over 250 charge-discharge cycles and a high peak power density of 119 mW cm^{-2} at a voltage of 0.578 V.

2. Experimental

2.1. Synthesis of Co-MOF/GO-N (N = 2, 4, 6, 8, and 10)

Graphene oxide (GO) was synthesized from graphite powder by a modified Hummers' method [34]. A 0.5 g GO was dispersed in 50 mL distilled water. A 1.3686 g 2-methylimidazole (2-MI) was dissolved in 15 mL distilled water and then added to the GO solution. 2-MI/GO powder was obtained by stirring the mixed solution at room temperature for 1 h, followed by centrifuging and washing with distilled water. Afterwards, 2-MI/GO powder was added to a cobalt acetate solution prepared by dissolving 0.4152 g cobalt acetate in 15 mL distilled water. The mixture was subjected to the same process including stirring, centrifuging, and washing as described above. The final product was obtained after drying the collected material at 85 °C under vacuum. The final product is denoted as Co-MOF/GO-1 as the graphene oxide was exposed to cobalt acetate and 2-MI solution once. Additional samples were prepared by using the same procedure described above, but exposing graphene oxide to cobalt acetate and 2-MI solution two, four, six, eight, and ten times. The as-produced samples are denoted as Co-MOF/GO-2, Co-MOF/GO-4, Co-MOF/GO-6, Co-MOF/GO-8, and Co-MOF/GO-10, respectively.

2.2. Synthesis of Co-N-C/rGO-10-T (T = 450, 500, 600 and 800 °C)

The Co-N-C/rGO-10-*T* samples (rGO is reduced GO) were prepared using a direct carbonization process by heating Co-MOF/GO-10 sample at 450, 500, 600, and 800 °C, for 5 h at a heating rate of 10 °C min^{-1} under N_2. The as-produced samples are denoted as Co-N-C/rGO-10-450, Co-N-C/rGO-10-500, Co-N-C/rGO-10-600, and Co-N-C/rGO-10-800, respectively. Co-N-C/rGO-*N*-600 (*N* = 2, 4, 6, and 8) sample was synthesized by carbonizing Co-MOF/GO-*N* (*N* = 2, 4, 6, and 8) sample at 600 °C for 5 h with a heating rate of 10 °C min^{-1} under N_2.

2.3. Material characterization

The X-ray diffraction (XRD) patterns were collected on a Cu Kα (λ = 0.1541 nm) radiation source (D/MAX-RB RU-200B). Transmission electron microscopy (TEM) and high resolution TEM (HR-TEM) were performed on a JEM2010-HR microscope (FEI Tecnai G2 F30). Scanning electron microscope (SEM) images were obtained on a Zeiss Ultra Plus instrument. Raman spectroscopy was used to study the degree of graphitization using a 633 nm laser source (INVIA/INVIA). Brunauer-Emmett-Teller (BET) surface area analysis was performed by nitrogen physisorption at 77 K on an ASAP 2020 instrument. X-ray photoelectron spectroscopy (XPS) was employed to probe the chemical state of each element on a VG Multilab 2000X-spectrometer using an Al Kα X-ray source (1,486 eV). Quartz crystal microbalance with dissipation (QCM-D, Q-Sense E1, Sweden) was used to reveal the real-time frequency and dissipation change after the excitation of the freely oscillating quartz crystal. Thermogravimetric (TG) and differential thermal gravimetric analysis (DTG) data were recorded on a Discovery TGA thermal analysis system in N_2 at a heating rate of 10 °C min^{-1}.

2.4. Electrochemical characterization

Electrochemical measurements were performed on a standard three-electrode system (CHI660E, CHI instrument) using RHE as a reference electrode, Pt as a counter electrode, and the catalyst coated rotating disk electrode as a working electrode. The catalyst ink was prepared by dispersing the catalyst in a mixed solution containing 0.8 mL isopropanol, 20 μL Nafion solution (5 wt%, Dupont), and 0.2 mL distilled water. The ORR/OER tests were conducted on a rotating-disk electrode system with a rotational speed ranging from 400 to 2,000 r min^{-1} at a scan rate of 5 mV s^{-1}. 0.1 mol L^{-1} KOH was used as an electrolyte, which was bubbled with N_2 or O_2 for ~30 min prior to the measurements. The ORR stability test was carried out at 0.55 V (vs. RHE) in an O_2-saturated 0.1 mol L^{-1} KOH solution. In order to measure the catalytic performance for Zn-air battery application, electrodes were fabricated by mixing the catalyst with polyvinylidene fluoride (PVDF) and acetylene carbon at a weight ratio of 8:1:1 in *N*-methyl pyrrolidone (NMP) solution. The resulting slurry was homogeneously dispersed on the hydrophobic carbon paper and dried at 85 °C for 2 h. The electrode mass loading in a Zn-air battery was 3 mg cm^{-2}. A Zn foil was used as an anode and 6 mol L^{-1} KOH with 0.2 mol L^{-1} zinc acetate as an electrolyte.

3. Results and discussion

The synthesis procedure for Co-N-C/graphene samples is illustrated in Fig. 1a. Co-MOF was used owing to its Co-N moieties, high nitrogen content and large specific surface area [35–38]. Co-MOF was assembled on the surface of GO through a layer-by-layer self-assembly process as outlined in the experimental section. Co-MOF/GO compound was formed by mixing GO with cobalt acetate solution and 2-MI multiple times. The organic ligand of Co-MOF interacts with GO by strong electrostatic attraction, leading to immobilized Co-MOF on GO. During the carbonization process, Co-MOF and GO are converted to N-doped porous carbon and reduced graphene oxide (rGO), respectively. The existence of Co-N-C structure and N-functionalized groups in the carbon framework is vital to enhance the ORR/OER catalytic activity [39]. And rGO nanosheets provide excellent conductivity, facilitating electron transport between catalytic reaction sites and the external circuit [25].

QCM-D measurements were conducted to investigate the adsorption of Co-MOF on the GO substrate. The shift in frequency and change in energy dissipation are effective to characterize the adsorption process [40]. GO substrate in water is negatively charged and 2-MI in water has a positive charge [41], which leads to an electrostatic attraction when 2-MI is deposited on GO surface. As shown in Fig. 1b, Δf reflects the change in mass as the oscillation frequency of the sensor is dependent on the mass adsorbed on its surface. An increase in mass (more negatively measured shift in QCM) suggests the successful self-assembly of Co-MOF on GO substrate. During the initial assembly of 2-MI, the adsorption was rapid, with a relatively constant value observed at ~15 min. In the subsequent assemblies of cobalt acetate, approximately 2 h was needed to reach a constant value, suggesting the organic ligand and metal ions of Co-MOF assembled through covalent bonding. After the deposition of Co-MOF layer, the adsorption effect of GO was impaired, instead, a decrease in mass uptake was noticed, likely due to the weakened electrostatic interaction when additional layers were deposited on the GO substrate.

TGA was conducted to monitor the weight loss of Co-N-C/rGO-10 from room temperature to 1,000 °C. As shown in Fig. 1c, the weight loss below 200 °C originated from the loss of moisture

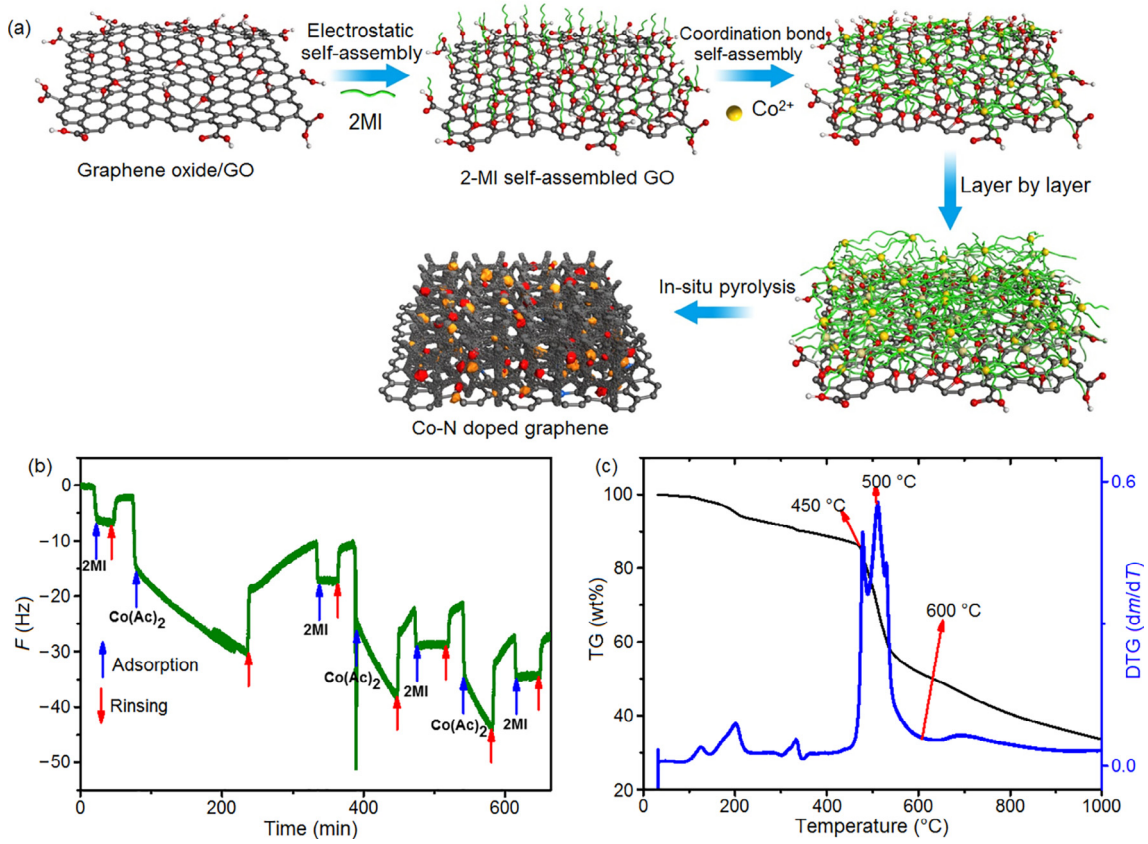

Fig. 1. (Color online) (a) Schematic of Co-N-C/graphene synthesis by self-assembly method. (b) Frequency and dissipation shifts for Co-MOF on GO substrate, blue and red arrow mark the adsorption of reacting liquid and rinsing with distilled water, respectively, and (c) TG (black) and DTG (blue) curves of Co-MOF/GO-10.

absorbed by the material [42]. A weight loss of approximately 7% was observed between 200 and 450 °C, owing to the decomposition of oxygen-containing functional groups on the GO substrate. The large mass decrease around 500 °C was attributed to the decomposition of Co-MOF, afterwards, the rate of weight loss remained relatively constant. Therefore, 450, 500, 600, and 800 °C were selected as the calcination temperatures for Co-N-C/rGO-10 to study the effect of carbonization temperature on the physical and electrocatalytic properties.

The effect of carbonization temperature on the phase formation was investigated by XRD (Fig. 2a). Clearly, a broad peak in the 2θ range of 20°–30° was observed in the XRD patterns of all samples, indicating the formation of amorphous carbon during the carbonization process. Moreover, additional peaks were observed in the samples calcinated at a temperature ≥500 °C. Careful search and match of these peaks in the PDF database showed the consistency with CoO, as well as Co_3O_4. Reflections relating to CoO and Co_3O_4 phases became more intense when increasing the calcination temperature from 500 to 600 °C. Further increasing temperature to 800 °C resulted in the formation of Co metal at an expense of Co_3O_4 phase. Such phase conversion from Co_3O_4 to Co would lead to a negative effect on the electrocatalytic activity [43,44]. Meanwhile, XRD of Co-MOF/GO-*N* (*N* = 0, 2, 4, 6, 8 and 10) sample was also performed for comparison, indicating the combination of Co-MOF (ZIF-67) and GO (Fig. S1 online). The graphitic feature of the carbonization samples was investigated by Raman spectroscopy. Two characteristic bands of graphite were observed at 1,329 cm^{-1} (D-band) and 1,573 cm^{-1} (G-band) (Fig. 2b). The ratio of the integrated intensity (I_D/I_G) for the samples carbonized at various temperatures (450, 500, 600 and 800 °C) was calculated to be 1.08, 1.04, 0.99 and 1.00, showing a high degree of graphitization for the calcined samples, which was benificial for the improvement of the electrochemical performance.

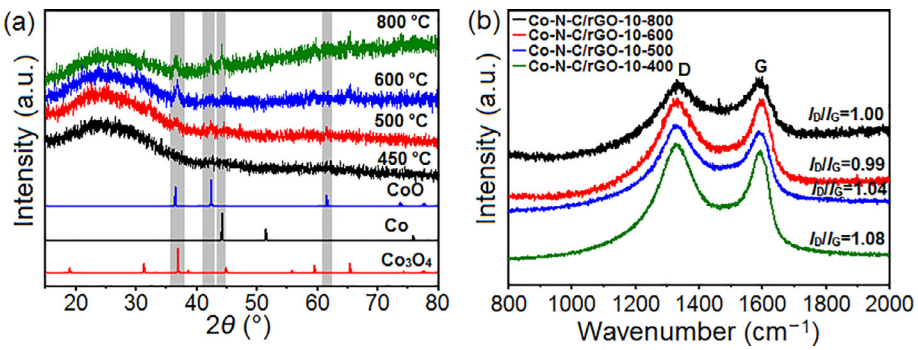

Fig. 2. (Color online) XRD (a) and Raman spectra (b) of Co-MOF/GO-10 carbonized at 450, 500, 600 and 800 °C. CoO (PDF No. 89-7099), Co (PDF No. 89-7093) and Co_3O_4 (PDF No. 74-1657) reference are shown for comparison.

The electrocatalytic ORR and OER activities of the samples were investigated in alkaline solution (0.1 mol L^{-1} KOH) with a standard three-electrode system. Samples were subjected to cyclic voltammetry (CV) scans for 100 cycles before the measurements to reach a stable state. The ORR and OER activity was evaluated via linear sweep voltammetry (LSV) at a scan rate of 5 mV s^{-1} (Fig. 3a). For comparison, the ORR and OER activity of a benchmark catalyst (20 wt% Pt/C) was also investigated under the same condition. We initially selected Co-N-C/rGO-10 to study the effect of carbonization temperature on the catalytic activity. Of all the samples calcinated at various temperatures, Co-N-C/rGO-10-600 showed the most positive ORR onset potential compared to other samples. Moreover, it appears to exhibit a high diffusion limiting current of 4.83 mA cm^{-2} for ORR at 1,600 r min^{-1}. The superior ORR activity for Co-N-C/rGO-10-600 sample is possibly due to the combined high degree of carbonization and less aggregation of metal oxide nanoparticles (NPs) in the final product (Fig. S2 online). We also investigated the influence of self-assembly numbers on the activities of the samples carbonized at 600 °C, but with different self-assembly layers (N = 2, 4, 6, 8 and 10) (Figs. S3 and S4 online). LSV curves of different samples at a potential scanning rate of 5 mV s^{-1} and rotating rate of 1,600 r min^{-1} are presented in Fig. 3b. Interestingly, the sample with 6 self-assembly layers (Co-N-C/rGO-6-600) exhibited the best catalytic activity, which outperforms the benchmark Pt/C catalyst. As shown in Fig. 3c, Co-N-C/rGO-6-600 sample exhibited an onset potential of 0.963 V

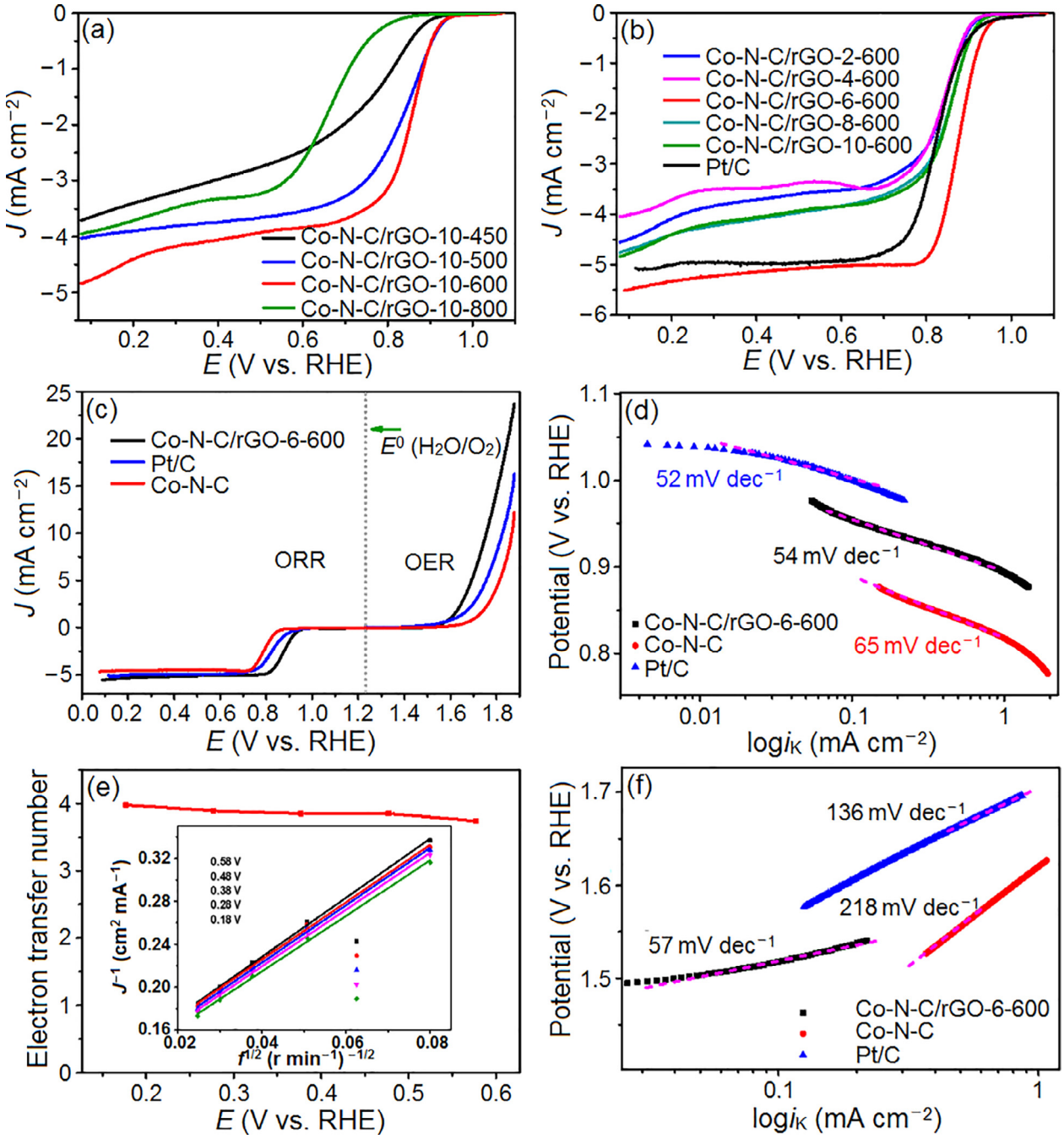

Fig. 3. (Color online) LSV curves of (a) Co-N-C/rGO-10-T (T = 450, 500, 600, and 800 °C) and (b) Co-N-C/rGO-N-600 (N = 2, 4, 6, 8 and 10). (c) ORR and OER polarization curves of Co-N-C, Co-N-C/rGO-6-600 and commercial Pt/C. (d) ORR Tafel plots obtained from the ORR polarization curves. (e) Calculated ORR electron-transfer number for Co-N-C/rGO-6-600 catalyst with an inset of Koutecky-Levich (K-L) plot at various potentials. (f) OER Tafel plots obtained from the OER polarization curves. All tests were performed in an O_2-saturated 0.1 mol L^{-1} KOH solution at 1,600 r min^{-1}.

and a diffusion limiting current of 5.5 mA cm^{-2} as well as a half-wave potential of 0.87 V, comparable to that of Pt/C electrode (0.81 V). Compared to pure Co-N-C, the onset potential of Co-N-C/rGO-6-600 showed a positive shift of 113 mV, and an increase of 0.8 mA cm^{-2} in ORR diffusion limiting current, which further confirms the contribution of rGO in combination with 3D porous structure to the electrochemical performance. It is noteworthy that Co-N-C/rGO-6-600 sample showed a similar Tafel slope (54 mV dec^{-1}) for ORR compared to that of Pt/C (52 mV dec^{-1}) in the low current density region (Fig. 3d), suggesting a similar kinetics in the rate-determined step during the ORR [45]. The electron-transfer number for the ORR was investigated by Koutecky-Levich (K-L) plots and calculated to be in the range of 3.74–3.98 (Fig. 3e), suggesting a four-electron reduction pathway for the major water product. Moreover, CV curve of Co-N-C/rGO-6-600 catalyst had no characteristic peak in the N_2-saturated KOH solution (Fig. S5a online), suggesting the good stability in the scanned electrochemical window. Prominent cathodic peaks were observed when saturating the alkaline electrolyte with O_2 (Fig. S5b online), increasing cathodic current with rotation speed suggested the improved mass transport to the electrode surface. All these results confirmed the good ORR performance of Co-N-C/rGO-6-600 catalyst under alkaline condition and the EIS curve of Co-N-C/rGO-6-600 catalyst was also tested in Fig. S6 (online). LSV curves of Co-N-C, Co-N-C/rGO-6-600, and Pt/C catalyst for OER were also collected in 0.1 mol L^{-1} KOH electrolyte. The potential at a current density of 10 mA cm^{-2} was used to evaluate the OER activity. Co-N-C/rGO-6-600 sample exhibited a potential of 1.72 V, comparable to that of RuO_2 (1.75 V) [38], but lower than that for Co-N-C (1.8 V) and Pt/C (1.94 V). The Tafel slope of Co-N-C/rGO-6-600 was 57 mV dec^{-1}, much smaller than that of Co-N-C (218 mV dec^{-1}) and Pt/C (136 mV dec^{-1}) (Fig. 3f), suggesting the OER reaction for Co-N-C/rGO-6-600 catalyst was kinetically faster. Therefore, Co-N-C/rGO-6-600 is potentially favorable to be used as a bi-functional catalyst.

One of the major limitations for noble metal based oxygen catalysts is its poor tolerance to fuels such as methanol and impurities. Here, we characterize the fuel tolerance of Co-N-C/rGO-6-600 by using methanol as a model fuel. The methanol tolerance was evaluated at a potential of 0.55 V (vs. RHE) with a rotating rate of 1,600 r min^{-1}. There was a sharp decrease in the reaction current for Pt/C catalyst after the addition of methanol to the electrolyte in 500 s. In contrast, Co-N-C/rGO-6-600 catalyst retained a stable current response with minimal performance loss (Fig. 4a). The long-term stability of Co-N-C/rGO-6-600 and commercial Pt/C catalyst for ORR were also studied by chronoamperometric measurements at 0.55 V (vs. RHE) in an O_2-saturated 0.1 mol L^{-1} KOH solution (Fig. 4b). 97% of its initial ORR reaction current was retained after 10,000 s for Co-N-C/rGO-6-600 catalyst while the Pt/C catalyst showed a 7% current loss under the same condition. These results confirmed that Co-N-C/rGO-6-600 catalyst had better stability than Pt/C catalyst, possibly due to its excellent 3D porous structure with metal oxide NPs embedded within the graphite carbon. This unique structure helps confine the metal oxide NPs and suppress their dissolution and aggregation, therefore preventing the loss of active sites [46].

To further characterize the morphology and nanostructure of the best performing Co-N-C/rGo-6-600 catalyst, SEM and TEM analysis were performed. Cobalt oxide NPs derived from MOF were homogenously embedded on the rGO sheets with no obvious detachment or aggregation (Fig. 5a, b) and their particle size was about 13–35 nm. HRTEM image (Fig. 5c) also shows the cobalt oxide NPs embedded in the carbon matrix. Lattice fringes of the inner core of CoO and Co_3O_4 NPs were consistent with the crystal structure, the [2 0 0] and [3 1 1] lattice fringes exhibiting an interspacing of 0.213 and 0.243 nm. TEM image of Co-N-C/rGO-6-600

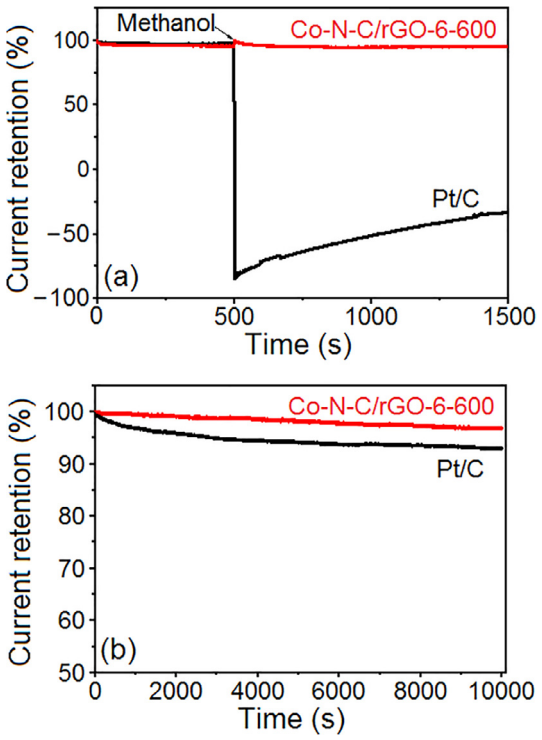

Fig. 4. (Color online) (a) Tolerance to methanol and (b) current retention of Co-N-C/rGO-6-600 and Pt/C electrodes recorded at 0.55 V vs. RHE in an O_2-saturated 0.1 mol L^{-1} KOH electrolyte at a rotation speed of 1,600 r min^{-1}.

(Fig. 5d) further confirmed that cobalt oxide NPs were uniformly distributed and immobilized on the surface of rGO nanosheet at a much smaller scale, showing consistency with SEM results. We also explored the spatial confinement of CoO_x NPs within a carbon shell, which is important to prevent the dissolution and aggregation of the metal oxide NPs under working condition. The elemental mapping presented in Fig. 5e–h showed the successful doping and uniform distribution of C, N, O and Co elements. The concentration line profiles of Co, C, N and O elements (Fig. 5i) confirmed the formation of Co-N/O-C moieties through the coordination of Co atoms after the calcination process.

Chemical state of each element in the as-produced Co-N-C/rGO-6-600 sample was further characterized by XPS, which confirmed the presence of C, N, and Co. The Co 2p spectrum could be fitted with three peaks (Fig. 6a) and the relative content of Co collected by XPS was about 0.37%. The appearance of Co–N peak (781.1 and 785.7 eV) provided concrete evidence for the formation of Co–N structures. The C 1s peak was deconvoluted into three different contributions at 285.7, 284.6 and 286.6 eV, corresponding to C—C, C=C and C—N/C—O, respectively (Fig. 6b). The N 1s peak can be deconvoluted into three peaks that are assigned to the pyridinic N (398.6 eV), pyrrolic N (399.7 eV) and graphite N (400.8 eV), supporting the incorporation of N into carbon matrix (Fig. 6c). Pyridinic N and pyrrolic N can easily coordinate with Co, forming Co-N active sites for ORR [47], and graphite N is also favorable for ORR due to the enhanced charge transfer rate [48]. Noteworthily, CoO_x NPs and the Co-N moieties constructed in the materials acting as the catalytic active sites can exhibit synergistically electrochemical performance for both ORR and OER. Nitrogen adsorption/desorption isotherms of Co-N-C/rGO-6-600 sample exhibited a typical type-IV adsorption/desorption behavior, suggesting the presence of a mesoporous structure (Fig. 6d). BET surface area of Co-N-C/rGO-6-600 was measured to be 252 m^2 g^{-1}. This pore size will enable the efficient exposure of the active sites with electrolyte and facilitate a rapid reaction [36].

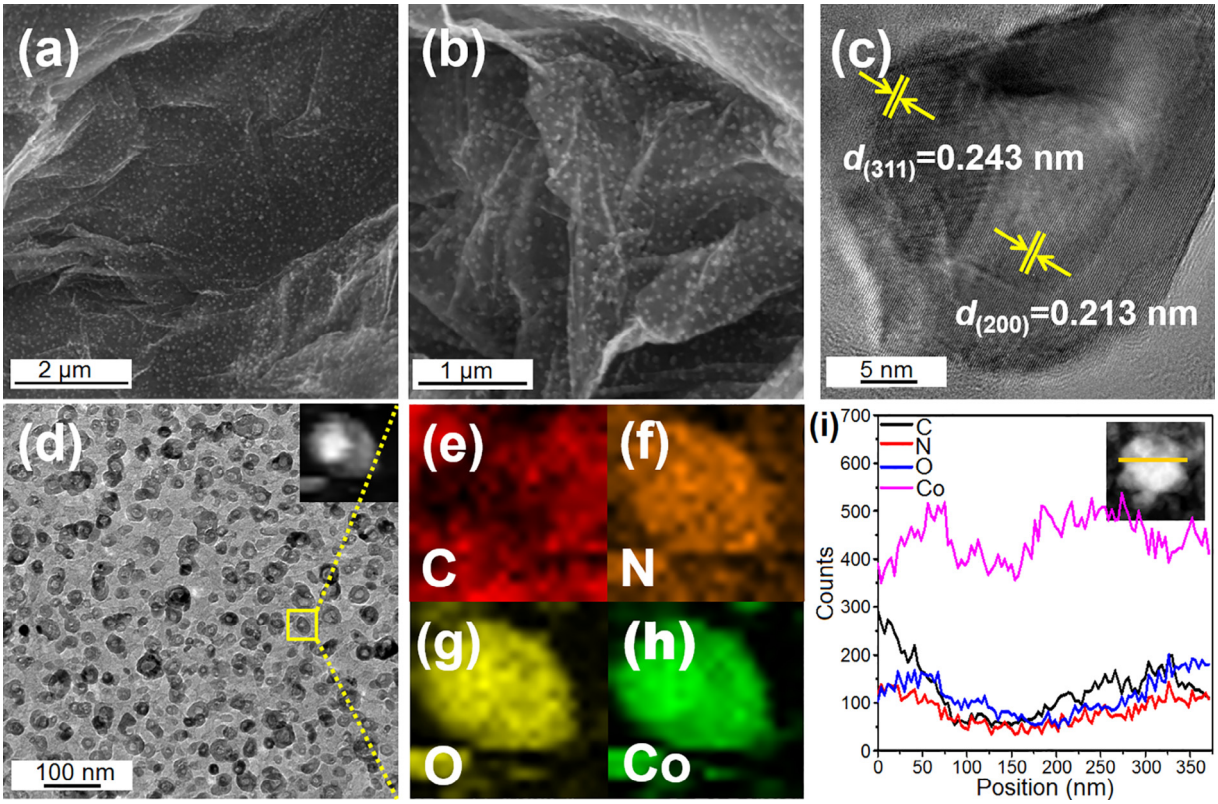

Fig. 5. (Color online) (a, b) SEM, (c, d) TEM, (e–h) elemental mapping, and (i) elemental line concentration profile of Co-N-C/rGO-6-600 catalyst. The inset in (i) shows the corresponding TEM image.

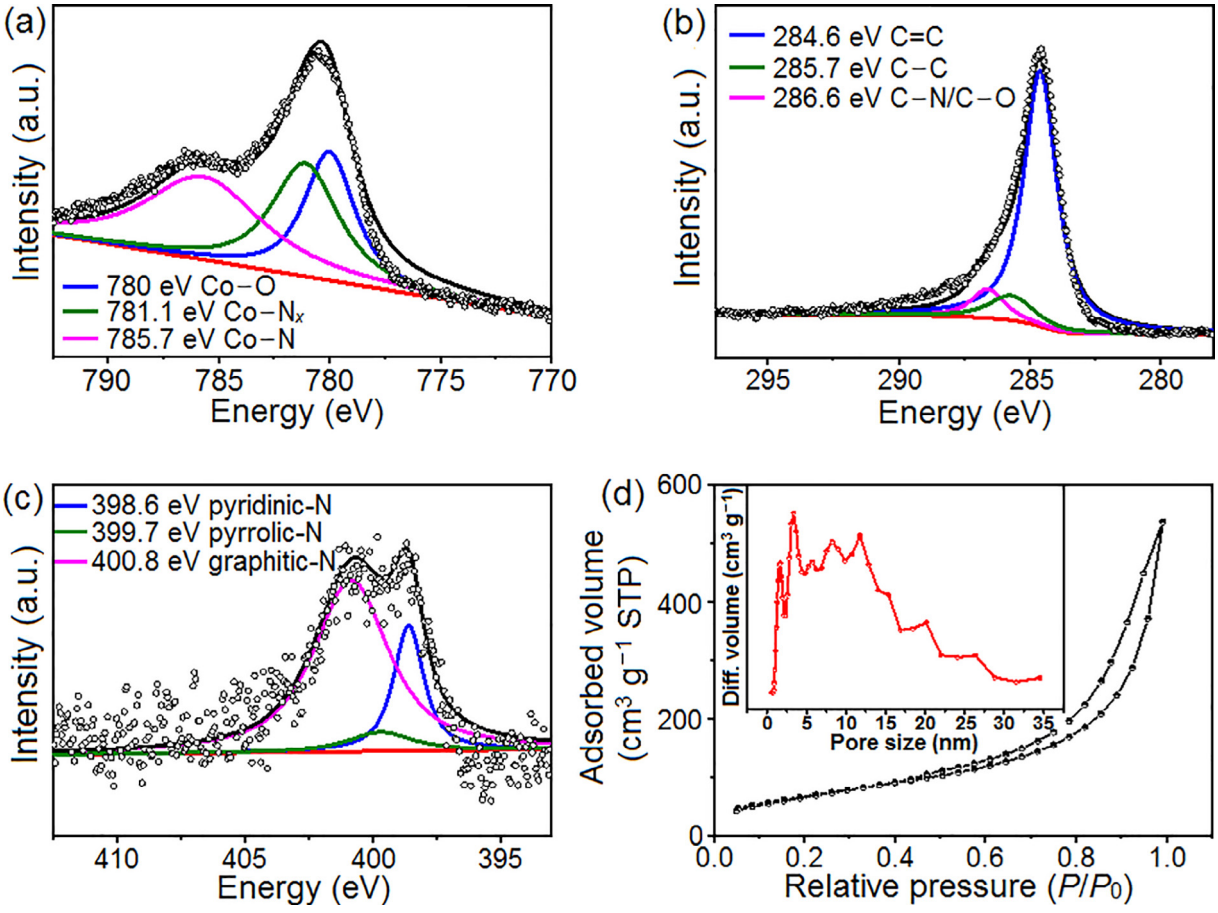

Fig. 6. (Color online) XPS spectra of (a) Co 2p, (b) C 1s, (c) N 1s and (d) nitrogen isothermal adsorption/desorption curves of Co-N-C/rGO-6-600 catalyst.

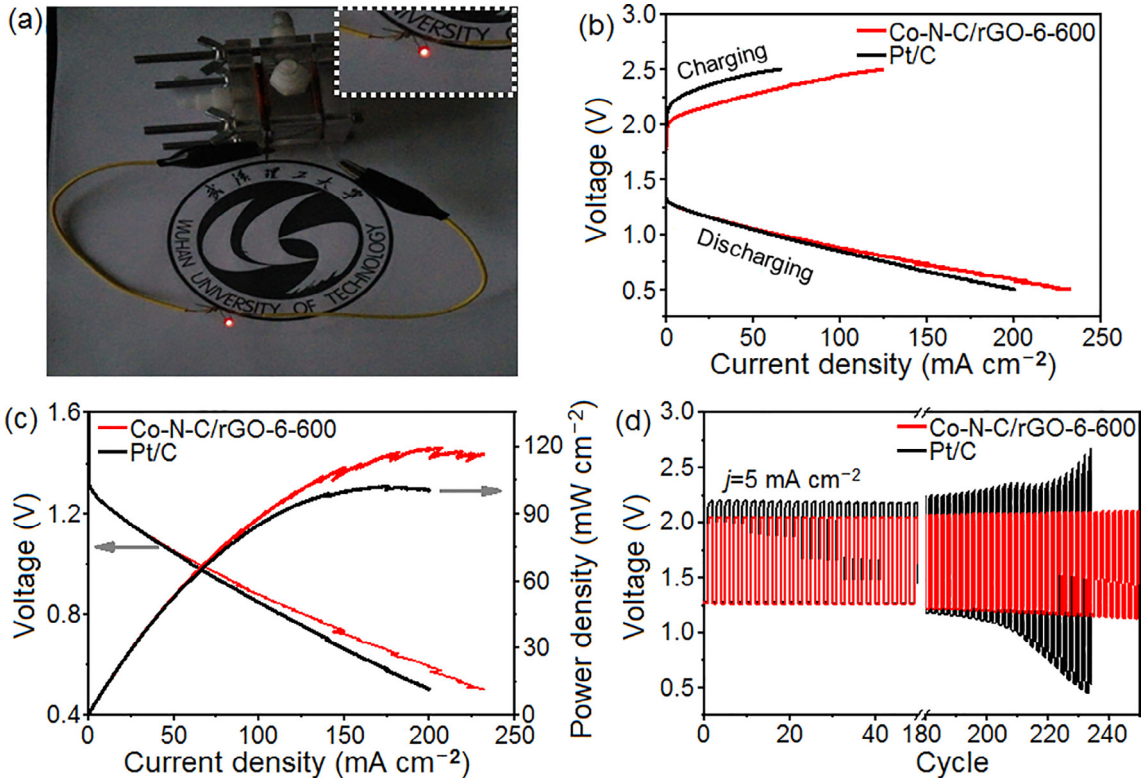

Fig. 7. (Color online) (a) Photograph of a red LED (~1.5 V) powered by a Zn-air battery. (b) Charge-discharge polarization curves of two-electrode Zn-air battery based on Co-N-C/rGO-6-600 catalyst. (c) Polarization and power density curves and (d) cycling performance of rechargeable Zn-air batteries based on Co-N-C/rGO-6-600 and commercial Pt/C at 5 mA cm^{-2}. 200 s of charge-discharge time in (d) was used.

Finally, the bi-functional catalytic properties were evaluated in an operational Zn-air battery. A red light-emitting diode (LED, 1.5 V) was powered by a Zn-air battery with Co-N-C/rGO-6-600 catalyst as the air electrode (Fig. 7a), demonstrating a functional device based on Co-N-C/rGO-6-600 catalyst. Overall, the as-produced Co-N-C/rGO-6-600 catalyst exhibited a discharge and charge potential of 1.18 and 2.14 V at a current density of 20 mA cm^{-2} and a peak power density of 119 mW cm^{-2} at a voltage of 0.578 V, comparable to the benchmark Pt/C (Fig. 7b, c). And the Zn-air battery based on Co-N-C/rGO-6-600 catalyst exhibited much improved stability over the long-term cycling, as evidenced by a smaller voltage gap between charge and discharge than that of commercial Pt/C catalyst as well as minimal change in voltage over 250 cycles (Fig. 7d).

4. Conclusion

In conclusion, we report the synthesis of Co-N-C/graphene catalyst with 3D porous structure through layer-by-layer self-assembly method. This self-assembly approach is facile and efficient to fabricate 3D porous structure with desired composition and morphology. In the as-produced catalyst, the graphene substrate enhances the overall electrical conductivity, and cobalt oxide NPs function as active sites to expedite the ORR process. Additionally, the 3D porous electrode provides abundant channels and vacancies for improved mass transport and leads to an excellent ORR activity. Such a non-noble carbon based catalyst exhibits an onset potential of 0.963 V and half-wave potential of 0.87 V toward ORR as well as comparable OER performance to commercial RuO_2. Finally, potential application as a bi-functional catalyst is demonstrated in a functional device powered by a Zn-air battery based on the as-produced carbonaceous catalyst. Our results further highlight the potential promise to develop carbon based catalyst as bi-functional oxygen electrocatalyst for metal-air battery. In addition, the facile approach reported in this work is applicable to the further advancement of such electrocatalysts by tuning the composition and morphology.

Conflict of interest

The authors declare that they have no conflict of interest.

Acknowledgments

This work was supported by the National Natural Science Foundation of China (51472187). William M. Yourey greatly appreciates Penn State ETCE and Penn State Hazleton Research and Development Grants.

Author contributions

Shichang Cai performed the experiments and prepared the origin draft. Rui Wang performed the analysis with constructive discussions. William M. Yourey and Junsheng Li validated the draf. Haining Zhang reviewed and edited the draft. Haolin Tang contributed to the conception of the study.

Appendix A. Supplementary data

Supplementary data to this article can be found online at https://doi.org/10.1016/j.scib.2019.05.020.

References

[1] Debe MK. Electrocatalyst approaches and challenges for automotive fuel cells. Nature 2012;486:43–51.

[2] Zheng Y, Jiao Y, Jaroniec M, et al. Nanostructured metal-free electrochemical catalysts for highly efficient oxygen reduction. Small 2012;8:3550–66.
[3] Bu L, Ding J, Guo S, et al. A general method for multimetallic platinum alloy nanowires as highly active and stable oxygen reduction catalysts. Adv Mater 2015;27:7204–12.
[4] Gasteiger HA, Marković NM. Chemistry. Just a dream—or future reality? Science 2009;324:48–9.
[5] Bruijn FAD, Dam VAT, Janssen GJM. Review: durability and degradation issues of pem fuel cell components. Fuel Cells 2008;8:3–22.
[6] Xu N, Li X, Li H, et al. A novel composite (fmc) to serve as a durable 3D-clam-shaped bifunctional cathode catalyst for both primary and rechargeable zinc-air batteries. Sci Bull 2017;62:1216.
[7] Xia W, Mahmood A, Zou R, et al. Metal-organic frameworks and their derived nanostructures for electrochemical energy storage and conversion. Energy Environ Sci 2015;2015:1837–66.
[8] Jiao Y, Zheng Y, Jaroniec M, et al. Origin of the electrocatalytic oxygen reduction activity of graphene-based catalysts: a roadmap to achieve the best performance. J Am Chem Soc 2014;136:4394–403.
[9] Zheng Y, Jiao Y, Ge L, et al. Two-step boron and nitrogen doping in graphene for enhanced synergistic catalysis. Angew Chem Int Ed 2013;52:3110–6.
[10] Wang S, He P, Xie Z, et al. Tunable nanocotton-like amorphous ternary Ni-Co-B: a highly efficient catalyst for enhanced oxygen evolution reaction. Electrochim Acta 2019;296:644–52.
[11] Liu D, Tao L, Yan D, et al. Recent advances on non-precious metal porous carbon-based electrocatalysts for oxygen reduction reaction. ChemElectroChem 2018;5:1775–85.
[12] Gao X, Li X, Kong Z, et al. Bifunctional 3D n-doped porous carbon materials derived from paper towel for oxygen reduction reaction and supercapacitor. Sci Bull 2018;63:621.
[13] Zhu Y, Murali S, Cai W, et al. Graphene and graphene oxide: synthesis, properties, and applications. Adv Mater 2010;22:3906–24.
[14] Weiss NO, Zhou H, Liao L, et al. Graphene: an emerging electronic material. Adv Mater 2012;24:5782–825.
[15] Guo C, Liao W, Li Z, et al. Coprinus comatus-derived nitrogen-containing biocarbon electrocatalyst with the addition of self-generating graphene-like support for superior oxygen reduction reaction. Sci Bull 2016;61:948–53.
[16] Zheng Y, Jiao Y, Jaroniec M, et al. Nanostructured metal-free electrochemical catalysts for highly efficient oxygen reduction. Small 2012;8:3550–66.
[17] Luo B, Liu S, Zhi L. Chemical approaches toward graphene-based nanomaterials and their applications in energy-related areas. Small 2012;8:630–46.
[18] Shao Y, Zhang S, Wang C, et al. Highly durable graphene nanoplatelets supported pt nanocatalysts for oxygen reduction. J Power Sources 2010;195:4600–5.
[19] Parvez K, Yang S, Hernandez Y, et al. Nitrogen-doped graphene and its iron-based composite as efficient electrocatalysts for oxygen reduction reaction. ACS Nano 2012;6:9541–50.
[20] Jukk K, Kongi N, Rauwel P, et al. Platinum nanoparticles supported on nitrogen-doped graphene nanosheets as electrocatalysts for oxygen reduction reaction. Electrocatalysis 2016;7:428–40.
[21] Bayram E, Yilmaz G, Mukerjee S. A solution-based procedure for synthesis of nitrogen doped graphene as an efficient electrocatalyst for oxygen reduction reactions in acidic and alkaline electrolytes. Appl Catal B Environ 2016;192:26–34.
[22] Wang S, He P, Jia L, et al. Nanocoral-like composite of nickel selenide nanoparticles anchored on two-dimensional multi-layered graphitic carbon nitride: a highly efficient electrocatalyst for oxygen evolution reaction. Appl Catal B Environ 2019;243:463–9.
[23] Shen K, Chen X, Chen J, et al. Development of mof-derived carbon-based nanomaterials for efficient catalysis. ACS Catal 2016;6:5887–903.
[24] Shang L, Yu H, Huang X, et al. Well-dispersed zif-derived Co, N-co-doped carbon nanoframes through mesoporous-silica-protected calcination as efficient oxygen reduction electrocatalysts. Adv Mater 2016;28:1668–74.
[25] Yang J, Zhu G, Liu Y, et al. Fe_3O_4-decorated Co_9S_8 nanoparticles in situ grown on reduced graphene oxide: a new and efficient electrocatalyst for oxygen evolution reaction. Adv Funct Mater 2016;26:4712–21.
[26] Chaikittisilp W, Torad NL, Li C, et al. Synthesis of nanoporous carbon-cobalt-oxide hybrid electrocatalysts by thermal conversion of metal-organic frameworks. Chemistry 2014;20:4217–21.
[27] Jiao L, Wan G, Zhang R, et al. From metal-organic frameworks to single-atom fe implanted n-doped porous carbons: efficient oxygen reduction in both alkaline and acidic media. Angew Chem Int Ed 2018;57:8525–9.
[28] Tan B, Wu ZF, Xie ZL. Fine decoration of carbon nanotubes with metal organic frameworks for enhanced performance in supercapacitance and oxygen reduction reaction. Sci Bull 2017;62:1132.
[29] Hou Y, Wen Z, Cui S, et al. An advanced nitrogen-doped graphene/cobalt-embedded porous carbon polyhedron hybrid for efficient catalysis of oxygen reduction and water splitting. Adv Funct Mater 2015;25:872–82.
[30] Xing C, Liu Y, Su Y, et al. Structural evolution of co-based metal organic frameworks in pyrolysis for synthesis of core-shells on nanosheets: Co@CoO_x@carbon-rGO composites for enhanced hydrogen generation activity. ACS Appl Mater Interfaces 2016;8:15430–8.
[31] Jahan M, Liu Z, Loh KP. A graphene oxide and copper-centered metal organic framework composite as a tri-functional catalyst for HER, OER, and ORR. Adv Funct Mater 2013;23:5363–72.
[32] Versluis F, van Esch JH, Eelkema R. Synthetic self-assembled materials in biological environments. Adv Mater 2016;28:4576–92.
[33] Li M, Liu T, Fan L, et al. Three-dimensional hierarchical meso/macroporous Fe/co-nitrogen-doped carbon encapsulated FeCo alloy nanoparticles prepared without any template or surfactant: high-performance bifunctional oxygen electrodes. J Alloys Compd 2016;686:467–78.
[34] Marcano DC, Kosynkin DV, Berlin JM, et al. Improved synthesis of graphene oxide. ACS Nano 2010;4:4806–14.
[35] Chen B, Li R, Ma G, et al. Cobalt sulfide/N, S codoped porous carbon core-shell nanocomposites as superior bifunctional electrocatalysts for oxygen reduction and evolution reactions. Nanoscale 2015;7:20674–84.
[36] You B, Jiang N, Sheng M, et al. High-performance overall water splitting electrocatalysts derived from cobalt-based metal-organic frameworks. Chem Mater 2015;27:7636–42.
[37] Aijaz A, Masa J, Rosler C, et al. Co@Co_3O_4 encapsulated in carbon nanotube-grafted nitrogen-doped carbon polyhedra as an advanced bifunctional oxygen electrode. Angew Chem 2016;55:4087–91.
[38] Wang X, Zhou J, Fu H, et al. Mof derived catalysts for electrochemical oxygen reduction. J Mater Chem A 2014;2:14064–70.
[39] Chen Z, Wang Q, Zhang X, et al. N-doped defective carbon with trace co for efficient rechargeable liquid electrolyte-/all-solid-state Zn-air batteries. Sci Bull 2018;63:548–50.
[40] Boisse BMD, Liu G, Ma J, et al. Intermediate honeycomb ordering to trigger oxygen redox chemistry in layered battery electrode. Nat Commun 2016;7:11397–405.
[41] Chen D, Feng H, Li J. Graphene oxide: preparation, functionalization, and electrochemical applications. Chem Rev 2012;112:6027–53.
[42] Yao X, Guo G, Zhao Y, et al. Synergistic effect of mesoporous Co_3O_4 nanowires confined by n-doped graphene aerogel for enhanced lithium storage. Small 2016;12:3849–60.
[43] Zhang M, Huang YL, Wang JW, et al. A facile method for the synthesis of a porous cobalt oxide–carbon hybrid as a highly efficient water oxidation catalyst. J Mater Chem A 2016;4:1819–27.
[44] Uhlig LM, Sievers G, Brüser V, et al. Characterization of different plasma-treated cobalt oxide catalysts for oxygen reduction reaction in alkaline media. Sci Bull 2016;61:612–8.
[45] Liu X, Liu W, Ko M, et al. Metal (Ni, Co)-metal oxides/graphene nanocomposites as multifunctional electrocatalysts. Adv Funct Mater 2015;25:5799–808.
[46] Tang H, Cai S, Xie S, et al. Metal-organic-framework-derived dual metal- and nitrogen-doped carbon as efficient and robust oxygen reduction reaction catalysts for microbial fuel cells. Adv Sci 2016;3:1487–98.
[47] Wei J, Hu Y, Liang Y, et al. Electrocatalysts: nitrogen-doped nanoporous carbon/graphene nano-sandwiches: synthesis and application for efficient oxygen reduction. Adv Funct Mater 2015;25:5768–77.
[48] Wu G, Zelenay P. Nanostructured nonprecious metal catalysts for oxygen reduction reaction. ACC Chem Res 2013;46:1878–89.

Shichang Cai earned his bachelor degree in 2013 from Henan University of Science and Technology and master degree in 2016 at the State Key Laboratory of Advanced Technology for Materials Synthesis and Processing in Wuhan University of Technology. He has continued his Ph.D. degree at State Key Laboratory of Advanced Technology for Materials Synthesis and Processing in Wuhan University of Technology until now. His research interests are focused on electrocatalysts, fuel cells, and metal-air batteries.

Haolin Tang earned his Ph.D. degree in Material Science from Wuhan University of Technology in 2007. Then he worked as a Research Fellow at Nanyang Technological University for a year, and in 2011 he was appointed as a full professor of the State Key Laboratory of Advanced Technology for Materials Synthesis and Processing in Wuhan University of Technology. His research interests include fuel cells, electrochemistry of nanomaterials, and self-assembly of nanocomposites.